Retinal polarization-sensitive optical coherence tomography at 1060 nm with 350 kHz A-scan rate using an Fourier domain mode locked laser

Teresa Torzicky
Sebastian Marschall
Michael Pircher
Bernhard Baumann
Marco Bonesi
Stefan Zotter
Erich Götzinger
Wolfgang Trasischker
Thomas Klein
Wolfgang Wieser
Benjamin Biedermann
Robert Huber
Peter Andersen
Christoph K. Hitzenberger

SPIE

Retinal polarization-sensitive optical coherence tomography at 1060 nm with 350 kHz A-scan rate using an Fourier domain mode locked laser

Teresa Torzicky,[a] **Sebastian Marschall,**[b] **Michael Pircher,**[a] **Bernhard Baumann,**[a] **Marco Bonesi,**[a] **Stefan Zotter,**[a] **Erich Götzinger,**[a] **Wolfgang Trasischker,**[a] **Thomas Klein,**[c] **Wolfgang Wieser,**[c] **Benjamin Biedermann,**[c] **Robert Huber,**[c] **Peter Andersen,**[b] **and Christoph K. Hitzenberger**[a]

[a]Medical University of Vienna, Center for Medical Physics and Biomedical Engineering, Austria
[b]Technical University of Denmark, DTU Fotonik, Department of Photonics Engineering, Denmark
[c]Ludwig-Maximilians-University Munich, Lehrstuhl für BioMolekulare Optik, Fakultät für Physik, Germany

Abstract. We present a novel, high-speed, polarization-sensitive, optical coherence tomography set-up for retinal imaging operating at a central wavelength of 1060 nm which was tested for *in vivo* imaging in healthy human volunteers. We use the system in combination with a Fourier domain mode locked laser with active spectral shaping which enables the use of forward and backward sweep in order to double the imaging speed without a buffering stage. With this approach and with a custom designed data acquisition system, we show polarization-sensitive imaging with an A-scan rate of 350 kHz. The acquired three-dimensional data sets of healthy human volunteers show different polarization characteristics in the eye, such as depolarization in the retinal pigment epithelium and birefringence in retinal nerve fiber layer and sclera. The increased speed allows imaging of large volumes with reduced motion artifacts. Moreover, averaging several two-dimensional frames allows the generation of high-definition B-scans without the use of an eye-tracking system. The increased penetration depth of the system, which is caused by the longer probing beam wavelength, is beneficial for imaging choroidal and scleral structures and allows automated segmentation of these layers based on their polarization characteristics. © *The Authors. Published by SPIE under a Creative Commons Attribution 3.0 Unported License. Distribution or reproduction of this work in whole or in part requires full attribution of the original publication, including its DOI.* [DOI: 10.1117/1.JBO.18.2.026008]

Keywords: optical coherence tomography; retinal imaging; spectral shaping; choroid; sclera; swept source; Fourier domain mode locking; polarization-sensitive; high-speed.

Paper 12497 received Aug. 6, 2012; revised manuscript received Dec. 18, 2012; accepted for publication Jan. 2, 2013; published online Feb. 1, 2013.

1 Introduction

Optical coherence tomography (OCT) is a noninvasive imaging technique for recording high-resolution images of biological samples and has been established, in ophthalmology, as a standard tool for diagnosing ocular diseases and for monitoring therapeutic success.[1–6] The essential step, which improved the technology to a state where it gained interest for clinical use in ophthalmology, was the introduction of the spectral-domain detection principle which increased acquisition speed and sensitivity in comparison to the former time-domain technology.[7–9]

Currently, state-of-the-art, commercially available retinal OCT scanners for clinical use work at a central wavelength of 840 nm and allow the acquisition of high depth resolution ($\sim$5 μm) images of the ocular fundus from the inner retinal layers to the retinal pigment ephitelium (RPE) with A-scan rates beyond 20 kHz. These devices are valuable tools for clinical examinations and provide additional information for the diagnostics of different retinal pathologies.[6]

However, there are three main limiting factors for extending the use of OCT for acquiring clinically relevant information with these state-of-the-art retinal OCT scanners. These limiting factors include slow acquisition speed which limits the maximum size of the volume that can be imaged with reduced motion artifacts, low penetration depth which determines the retinal layers that can be examined and which is mainly limited by absorption and scattering of the probing beam in the tissue, and lack of tissue specific contrast which cannot be obtained with state-of-the-art retinal scanners since the acquired information is based on backscattered intensity only.

With custom-built research OCT set-ups for retinal imaging, A-scan rates up to $\sim$310 and 500 kHz can be achieved with high-speed spectrometer based systems, up to 200 kHz with swept source set-ups using commercially available sources and even up to $\sim$1.68 MHz with a Fourier domain mode locked (FDML) laser.[10–14] Acquisition speed can be further increased with multispot approaches, however, the usability of such devices in clinical retinal imaging still needs to be examined.[12] However, at the moment, there are several indications that the next generation of commercial retinal scanners will work with acquisition speeds in the $\sim$100 kHz range.

Imaging speeds of $\sim$100 kHz are beneficial, on the one hand, for acquiring large densely sampled three-dimensional (3-D) data sets with reduced motion artifacts and, on the other hand, for generating high-definition two-dimensional (2-D) scans by averaging several frames without the use of an eye tracking device. The acquisition of large densely sampled 3-D volumes is especially interesting for the examination of patients with large pathological changes in the retina like geographic atrophies, pigment epithelial detachments, etc., since the whole pathological area can be imaged at once. Additionally, examination of fine features like micro exudates and small

drusen is improved due to the dense isotropic coverage of the measured volume. High-definition 2-D scans are advantageous because the signal-to-noise ratio is increased and the speckle contrast is reduced which improves the visibility of small structures with low contrast.[15,16]

The penetration depth, in retinal OCT imaging, can be increased by using longer probing wavelengths that are less scattered and absorbed in the RPE which enables the examination of deeper layers in the ocular fundus.[17–19] For this purpose, the wavelength range around 1060 nm is particularly suitable because water, the main constituent of the vitreous, has a local absorption minimum in that range and dispersion is minimal as well.[20–22] Increased penetration, in retinal OCT imaging, is of high interest since recent studies suggest that parameters like choroidal thickness or, more generally, pathological changes in the choroid might be suitable parameters for early diagnosis of several retinal diseases.[23–25] Therefore, diagnostic devices that allow examination of choroid and sclera might provide promising tools for the early diagnoses of retinal diseases and, additionally, for the general study of these layers *in vivo*.

Tissue specific contrast can be obtained by using polarization-sensitive OCT (PS-OCT), a functional extension of OCT.[26–28] PS-OCT has been shown to be a useful device for acquiring not only structural information from biological tissue but, additionally, information about the polarizing properties which enables the identification of different retinal layers due to their polarization characteristics.[29] So far, it is known that, in the posterior eye, the retinal nerve fiber layer, Henle's fiber layer, and the sclera show birefringence.[30–35] Additionally, certain layers show depolarizing characteristics including the RPE and other pigmented tissues like melanoma or naevi.[36,37] This additional information can be used for segmentation of different retinal layers based on tissue specific intrinsic contrast which has been shown to be a valuable tool in clinical diagnostics for the examination of pathologies involving the RPE.[38] Additionally, the polarization information, acquired by PS-OCT, allows more precise automated segmentation which does not suffer from the drawbacks that occur with manual segmentation approaches. Automated segmentation algorithms, based on PS-OCT data for the RPE and the choroidal scleral interface (CSI), have been demonstrated which, in combination, enable precise measurement of choroidal thickness.[39–41]

In this study, we present a high-speed swept source PS-OCT system in conjunction with a broadband FDML laser operating in the 1060 nm range with 350 kHz A-scan rate. The two-channel system acquires the data for both orthogonal polarization states simultaneously during each A-scan. Modulation of the drive current of the FDML laser permits optimizing the spectral shape and using both sweep directions for OCT imaging. These features enable, to the best of our knowledge, the fastest acquisition of PS-OCT data reported to date. During *in vivo* measurements in healthy human volunteers, we achieved high axial resolution and deep penetration into the choroid and the sclera. We demonstrate fast acquisition of large 3-D datasets and, additionally, high-definition 2-D images which permit precise automated segmentation of the RPE and the CSI within 2-D frames.

2 Methods

The work, presented in this paper, combines two special features. The arbitrary spectral shaping capability of the FDML laser permits the use of both sweep directions for OCT imaging. Hence, we can double the imaging speed without a buffering

stage as demonstrated in Ref. 42 while keeping the complexity of the optical set-up as low as possible. Secondly, we introduced a PS-OCT set-up, especially designed for large-field, high-speed polarization-sensitive imaging in the eye, which exploits the full imaging speed of the presented light source.

2.1 Light Source

The swept source set-up (Fig. 1) is a standard FDML ring-resonator comprising a single SOA (Exalos ESO330004), a Fabry-Perot tunable filter (Lambda Quest) with 180 pm linewidth full-width-half-maximum (FWHM), and a 1155 m long delay line made of standard single-mode fiber (Corning SMF28). Even though the single mode cut-off wavelength of SMF28 is specified to ~1250 nm, making it not true single mode fiber at 1050 nm, the coupling into higher order modes is sufficiently low as reported in Ref. 43. The resulting resonator round-trip frequency matches the maximum feasible operating frequency of the tunable filter, 175 kHz. Broadband isolators ensure unidirectional lasing and eliminate back reflections from the imaging interferometer into the FDML laser. A polarization controller corrects for polarization rotation in the fibers. Seventy percent of the light is coupled out of the resonator.

We operate the SOA with a custom diode driver (Wieserlabs WL-LDC10D) that permits modulation of the pump current with 15 MHz analog bandwidth. The tunable filter drive signal (sine wave and bias) as well as the current modulation waveform are synthesized by an arbitrary waveform generator controlled by a computer. The computer receives the signal from a 125 MHz photodetector for monitoring the instantaneous output power of the light source. With a LabView program running on the computer, we have full control over the tunable filter and the SOA current, power monitoring, spectral shaping, and automatic correction of the tunable filter bias.

For shaping the light source spectrum, we use an iterative algorithm similar to the one described in Ref. 44. This algorithm records the sweep intensity from the photodetector as input data and it can upload waveform data for the current modulation to the waveform generator. Starting with constant current, the algorithm compares the photodetector signal with the target shape and accordingly adjusts the modulation waveform. This step is repeated until the integrated difference between actual shape and target shape falls below a preset threshold. The algorithm finishes typically after five to 10 iterations, each taking approximately 3 s.
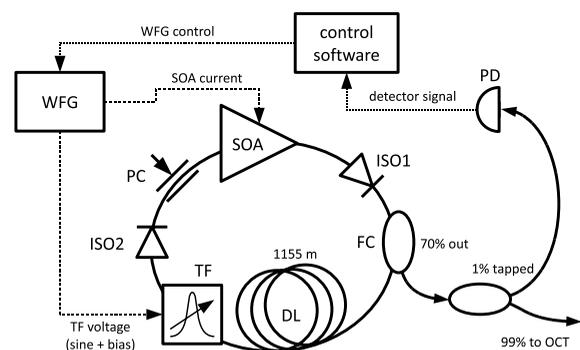

Fig. 1 Set-up of FDML Source, SOA: semiconductor optical amplifier, FC: fiber coupler, DL: delay line, ISO: optical isolator, TF: tunable filter, PC: polarization controller, WFG: waveform generator, PD: photodetector.

Once the current modulation waveform has been calculated, a stable sweep of the tunable filter is crucial. Otherwise, a slow shift of the sweep range, caused by thermal drift of the piezo-actuators, would, within a few minutes, lead to a strong distortion of the spectral shape. We compensate for the drift with an algorithm that automatically adjusts the filter bias voltage, thereby, enabling hands-off operation of the swept source over an extended period. After spectral shaping, the bias control algorithm continues to monitor the instantaneous power of the light source and detects deviations from the target shape. From the difference, it calculates an error value which it minimizes by adjusting the filter bias voltage using one channel of the waveform generator. With this implementation, we need no additional hardware for the bias control because we are already using the photodetector and the waveform generator for spectral shaping.

When the bias control is active, the laser can operate unattended until readjustment of the polarization controller becomes necessary. Depending on variations of the ambient temperature, these intervals range from 20 to 30 min.

With a constant pump current of 270 mA, the light source can support continuous lasing over a total sweep range up to 100 nm with an average output power of 10 to 15 mW. The sweep spectrum is centered, approximately at 1065 nm, and coincides perfectly with the local minimum in the water absorption spectrum which is important for maintaining high axial resolution.[20] The power spectrum has a peak on the long-wavelength side and a flat tail extending to the short wavelengths [Fig. 2(a)] which is typical for SOA-based swept sources. After linearization, the spectrum has a FWHM of ~55 nm and point spread functions, generated with this spectrum, yield a measured axial resolution of 12 μm in air [Fig. 2(c)]. The power difference between forward and backward sweep (i. e., from short to long wavelengths and vice versa) is relatively small. During the backward sweep (form long to short wavelengths) the peak power reaches about 90 percent of the forward sweep peak level [Fig. 2(a)]. By modulating the SOA pump current synchronously with the wavelength sweep, we can improve the actual axial resolution within a given total bandwidth by distributing the power more homogeneously over the sweep range. We achieve good results with a Gaussian shape on top of a constant baseline that ensures laser operation above threshold during the entire sweep. With a relatively high baseline (2/3 of total amplitude) [Fig. 2(b)] and

roughly the same average power as with constant current, we measured an axial resolution of nine μm in air [Fig. 2(c)].

After the spectral shaping, both sweep directions have equal power profiles and can both be used for OCT imaging. We measured a sensitivity of 95 to 96 dB with the forward sweep and about 94 dB with the backward sweep.

The sensitivity roll-off is relatively fast because the fiber resonator exhibits strong chromatic dispersion in the 1060 nm range.[45] At 1 mm probing depth, the roll-off is ~8 dB for the forward sweep and ~10 dB for the backward sweep. This residual asymmetry, between the two sweep directions, is a combined effect of the frequency-shift in the SOA and chromatic dispersion in the fiber resonator.

2.2 PS-OCT Set-Up

For high-speed polarization-sensitive imaging in the human eye, we used the PS-OCT set-up shown in Fig. 3. The design is similar to that in Refs. 41 and 46, but necessary adaptions were implemented in order to increase the data acquisition speed by a factor of 3.5 and to increase the scanning angle from ~20 deg to ~32 deg to image larger areas of the retina.

The presented PS-OCT set-up is based on a bulk-optics Mach-Zehnder configuration which allows balanced detection. A polarizer ensures a linear polarization state at the entrance of the interferometer. By the use of quarter and half wave plates, we generate a circular polarization state for illuminating the eye and a linear polarization state, rotated by 45 deg, returning from the reference arm. In general, the light returning from the sample is in an elliptically polarized state depending on the additional phase retardation that is accumulated while traversing the sample. This elliptical state interferes, in the second beam splitter cube, with the linear state from the reference arm and it is then coupled into two fiber-based polarizing beam splitters with polarization maintaining fibers. It is important that the fast axis of both fiber-based beam splitters is similarly oriented and complies with the orientation of the linear polarization state produced by the polarizer at the entrance of the interferometer. In the polarizing beam splitters, the polarization states are split into two orthogonal components which are, afterwards, simultaneously detected by two similar balanced detectors with a bandwidth of 350 MHz (Thorlabs PDB130C). For digitizing the signal, a 2-channel 12 bit data acquisition board, operating
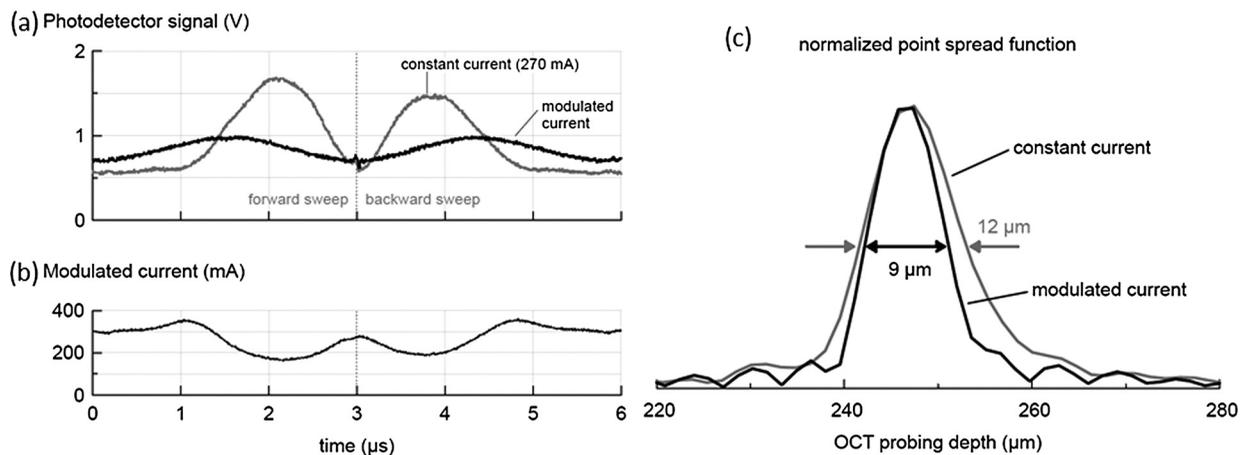

Fig. 2 Spectral shaping of forward and backward sweep of the FDML source: (a) Instantaneous power of forward and backward sweep at constant SOA current (gray trace) and at modulated SOA current (black trace); (b) modulated SOA current for spectral shaping; (c) resulting point spread functions with constant or modulated SOA current.
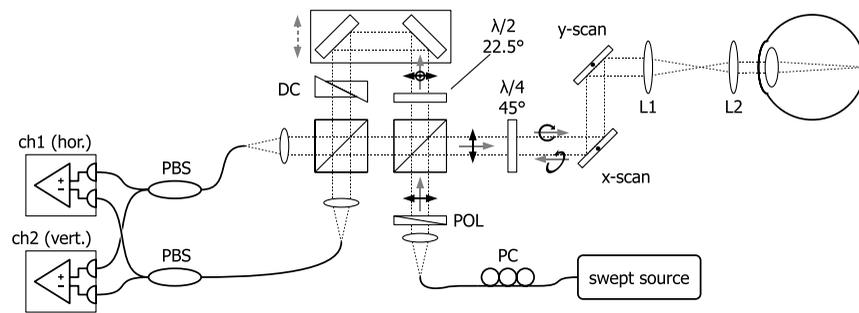
Fig. 3 Polarization sensitive optical coherence tomography set-up used for all images acquired, PC: polarization control, POL: polarizer, DC: dispersion compensation, PBS: polarizing beam splitter, L1: lense $f = 80$ mm, L2: lense $f = 50$ mm. For further details see description in the text.

at 500 MSamples/s, (AlazarTech) was used and controlled by custom-built LabView software. Additional parts, in the set-up, were a pair of prisms for hardware dispersion compensation in the reference arm and galvanometer scanners in the object arm which allowed scanning with a maximum angle of 20 deg when using lenses with equal focal lengths ($L1 = L2 = 50$ mm). For enabling raster scanning of larger areas, a telescope configuration of lenses with different focal lengths ($L1 = 80$ mm, $L2 = 50$ mm) were used enlarging the scan angle to 32 deg.

Since the Fabry-Perot tunable filter of the swept source was driven with a sinusoidal signal and no k-clocking was available for our custom built source, numerical rescaling of the raw signal was necessary. We calculated rescaling functions, for backwards and forwards sweep from signals, that were acquired from a common path interferometer before each measurement session.

For the images presented in this work, we illuminated the eye with ~1.8 mW which is consistent with the ANSI laser safety limits, providing a sensitivity of ~94 dB. Due to the relatively fast roll-off, only the first 2 mm of the imaging range provided suitable results for retinal imaging.

2.3 Imaging Protocol and Data Postprocessing

Two different imaging protocols were used to acquire the data presented in this paper. For acquiring the 3-D volumes and generating the intensity, retardation and fast axis cross-sections shown in Fig. 4, 200 B-scans were recorded, each consisting of 1000 A-scans. This covered a square of 32 deg×32 deg on the retina in only 0.65 s. With the second protocol, high-definition 2-D images of intensity, phase retardation, fast axis orientation and degree of polarization uniformity (DOPU) were generated by averaging over a B-scan series of 50 single frames (1000 A-scans per B-scan), acquired at the same position.[39] For averaging the polarization data, protocols described in Ref. 47 were used.

For both protocols, we performed standard Fourier domain OCT data preprocessing (fixed pattern noise removal, rescaling of the spectral data to remove sweep nonlinearities, spectral side lobe suppression by a Hanning window, zero padding, dispersion compensation) and an inverse fast Fourier transform (FFT). Afterwards, we used the resulting complex data sets (amplitude and phase information) from both channels for calculating reflectivity, retardation, optic axis orientation and DOPU values as described previously.[48,49]

The three healthy human volunteers, imaged with the described set-up, were informed about the nature and possible consequences of the study and consent was obtained. The study

was approved by the ethics committee of the Medical University of Vienna and adhered to the tenets of the Declaration of Helsinki.

3 Results

Three-dimensional and 2-D data sets of healthy human volunteers were acquired with the described polarization-sensitive OCT set-up and the described spectral shaping and imaging
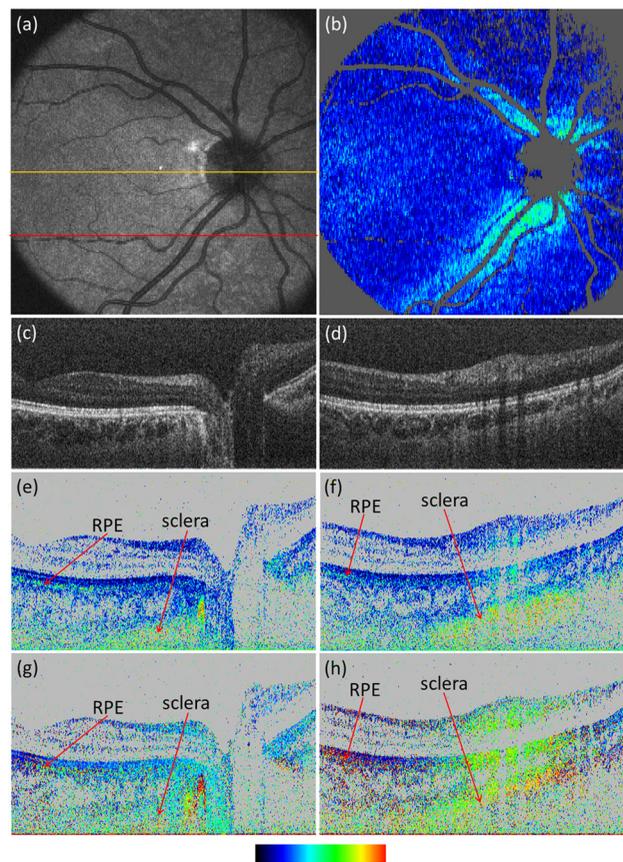

Fig. 4 3-D data set of the central retinal region of a healthy human volunteer acquired in 0.65 s. (200 B-scans, 1000 A-scans per B-scan, scanning angle ~32 deg×32 deg): (a) En face intensity image (log scale), yellow line: B-scans shown in (c), (e), (g); red line: B-scans shown in (d), (f), (h); (b) En face retardation image (scale bar 0 deg to 60 deg); (c) and (d) Intensity B-scan single frames (log scale); (e) and (f) Retardation B-scan single frames (scale bar: 0 deg to 90 deg); (g) and (h) Axis orientation B-scan single frames (scale bar: 0 deg to 180 deg). B-scan dimensions: 32 deg (horizontal) ×1 mm (vertical; geometric distance).

procedures. Figure 4 shows en face scans of intensity and retardation and B-scans of intensity, retardation, and axis orientation data taken from a 3-D volume which was acquired in 0.65 s. The intensity en face image in Fig. 4(a) shows the advantage of the high acquisition speeds since, even in such large volume, no motion artifacts are visible. The Fig. 4(c), 4(e), and 4(g) shows intensity, retardation, and fast axis orientation images from a central position of the 3-D data set which extends from the fovea to the optic nerve head [marked by the yellow line in Fig. 4(a)]. The typical polarization characteristics, such as the depolarization caused by the RPE and the birefringence of the sclera, are clearly visible in the retardation image 4(e) and the fast axis orientation image 4(g). B-scans from an inferior position [Fig. 4(d), 4(f), 4(h)] marked with the red line in 4(a), show in addition the birefringence of the retinal nerve fiber layer (RNFL). The birefringence of the RNFL can be even better visualized by generating en face retardation maps as shown in Fig. 4(b), where the thick nerve fiber bundles superior and inferior to the optic nerve head can be identified as areas with increased retardation, which is in good agreement with previous findings.[50–52] For generating retardation en face maps, segmentation of the RPE is performed based on DOPU values and only retardation values within a window above the RPE, which is mainly representing the junction between inner/outer segments of photoreceptors and the end tips of the photoreceptors are averaged.[39,50] Birefringence, caused by the anterior segment, is compensated using a software based algorithm described in detail elsewhere.[53]

For comparing the birefringence of the RNFL with previously published data, we additionally calculated quantitative birefringence values based on a method described in Refs. 31 and 54. The retardation values, within the RNFL, are plotted over the A-scan depth and with a linear fit, the slope of the retardation is determined and, thereby, the birefringence. In a second step, an annular area centered at the optic-nerve head, with an inner radius of approximately 1.3 mm and an outer radius of approximately 1.7 mm, is divided in four quadrants. The four quadrants are temporal (spanning an angle of 50 deg), superior (120 deg), nasal (70 deg), inferior (120 deg), and are the same quadrants as used for the temporal, superior, nasal, inferior, temporal diagrams of scanning laser polarimetry, a common tool in glaucoma diagnostics for examining the RNFL and its degradation. The used algorithm only delivers reliable data if the RNFL thickness is above a certain threshold, therefore, we decided to calculate quantitative data only for the superior and inferior quadrant. The birefringence values, within these sectors, were averaged over the respective A-scans. Birefringence values extracted for the superior and inferior region from the measurements performed in the three measured volunteers vary between 2.5×10^{-4} and 2.9×10^{-4}. This seems to be lower than the values that can be found in literature. Cense et al. reported in 2002 birefringence values of 4.5×10^{-4} near the optic nerve head region and, in a later work, he presented values ranging from 1.2 to 4.1×10^{-4} for different areas around the optic nerve head.[31,54] Yamanari et al. reported values from 1.2 to 6.3×10^{-4} around the optic nerve head and Mujat et al. reported an average birefringence of 3.04×10^{-4} for the RNFL.[51,55] Kemp et al. found values of 3.9×10^{-4} for RNFL birefringence in the inferior region measured in an anesthetized primate.[56] All values, mentioned here, were measured with PS-OCT set-ups working at a central wavelength of 840 nm. A recent paper also presents birefringence values, measured with a PS-OCT set-up, working at a central wavelength of 1060 nm.[57] The values are in range of 2.94 to 4.71×10^{-4} around the optic nerve head.

The discrepancies in the reported values could be caused by the different probing wavelengths or by variations in the RNFL birefringence between different subjects.

To investigate this further, we measured the three volunteers, additionally, with a PS-OCT set-up working at a central wavelength of 840 nm, which is described in detail in Ref. 58. In this case, averaged birefringence values, between 2.8 and 3.0×10^{-4}, were observed for the superior and inferior quadrants. Based on this comparison, one can conclude that there seems to be a trend towards slightly lower birefringence values in the superior and inferior quadrant at 1060 nm, however, the low number of measured subjects does not allow a definite conclusion.

Figure 5 shows high-definition 2-D scans of intensity, retardation, fast axis, and DOPU calculated from 50 single frames. The averaged images show reduced speckle characteristics and improved signal to noise ratio for the intensity [Fig. 5(a)], retardation [Fig. 5(b)], and fast axis orientation [Fig. 5(c)] values. Because the DOPU values [Fig. 5(d)] are calculated from the corresponding pixels in 50 frames instead of from a 2-D window that is moving within a single frame, we maintain nearly the full spatial resolution for the DOPU images.[47]

The depolarization in the DOPU image, in Fig. 5(d), seems less pronounced than in previously reported findings.[47,58] To further investigate if the difference is caused by the different probing wavelength, we examined DOPU images from the same subject acquired with PS-OCT set-ups working with different probing wavelengths. Since the imaging speed of the two set-ups is different (70 and 350 kHz), we decided to use the 2-D window method because, for this method, the window size for calculating the DOPU values can be better matched. Since DOPU values are statistic values, varying the window size can influence the DOPU values.

For a quantitative comparison, two areas of the same size and at the same spot within each DOPU image, were extracted and average DOPU values were calculated. One position was within the RPE directly in the fovea centralis where we observed average DOPU values of 0.5 for the 840 nm set-up and 0.74 for the set-up presented here. For a spot more nasal (5 deg from fovea centralis) on the RPE, we found averaged DOPU values of 0.64 (840 nm) and 0.78 (1060 nm).

There seems to be a trend to higher DOPU values (less depolarization) in the RPE for the 1060 nm set-up, however, more detailed studies in a larger study group are needed to support this preliminary finding.

Additionally, we applied an automated algorithm to the high-definition images, using polarization characteristics for segmenting the RPE and the choroid-scleral interface (CSI), for choroidal thickness measurements. The segmentation is performed using polarization data solely based on the procedures explained in Ref. 39. However, the data sequence used for averaging was acquired in 0.16 s (instead of 0.53 s), which is 3.3 times faster. Moreover, the scanning area was increased by a factor of 1.6 (32 deg instead of 20 deg). The resulting segmentation lines, generated by the algorithm, are drawn in the intensity [Fig. 5(e)] and retardation image [Fig. 5(f)]. In a second step, the choroidal thickness (ChT) was measured by calculating the distance between RPE and CSI. For the data
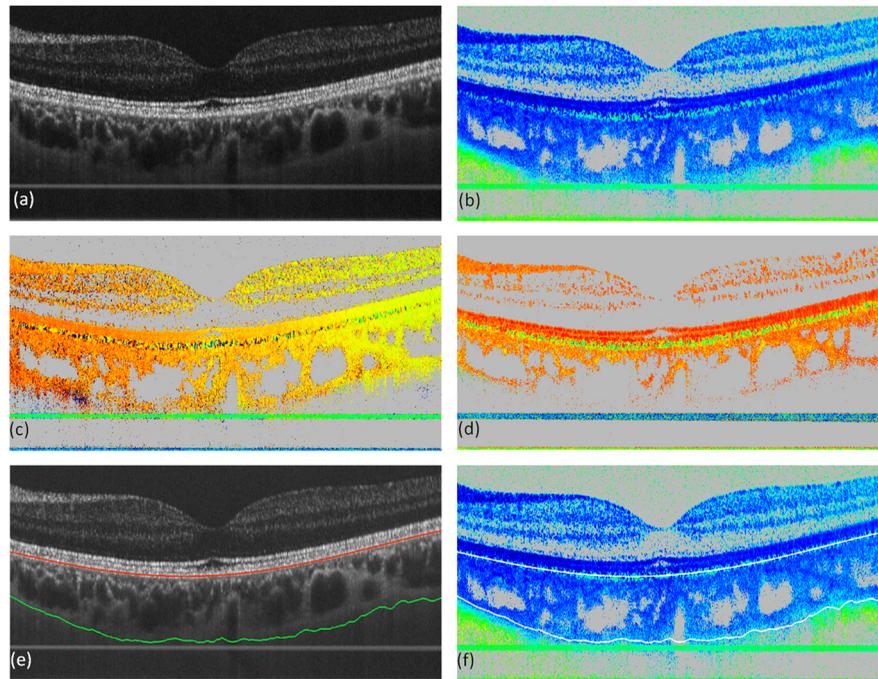
Fig. 5 Averaged 2-D data sets of the fovea of a healthy human volunteer. (50 frames averaged): (a) intensity image (log scale); (b) retardation image (scale bar 0 deg to 90 deg); (c) fast axis orientation (scale bar 0 deg to 180 deg); (d) degree of polarization uniformity B-scan (scale bar 0-1); (e) and (f) Segmentation of choroid based on PS-OCT data; (e) Intensity B-scans (red line: RPE, green line: CSI); (f) Retardation B-scans (top white line: RPE, bottom white line: CSI; scale bar 0 deg to 90 deg). B-scan dimensions: 32 deg (horizontal) ×1 mm (vertical; geometric distance).

set presented here, the mean ChT was 360 μm, which is in good agreement with the ChT measurement of the same subject performed with the set-up presented in Ref. 41.

4 Conclusion

We developed a high-speed swept source PS-OCT system operating at 1060 nm in combination with an FDML laser that enables an A-scan rate of 350 kHz. By acquiring *in vivo* retinal images of healthy human volunteers, we demonstrate the feasibility of the set-up for high-speed retinal PS-OCT measurements.

The high imaging speed allows generating 3-D data sets with less motion artifacts and the wavelength around 1060 nm which is particularly well suited for imaging polarization characteristics of deeper layers beneath the RPE. Even in single frames, the birefringence of the sclera is clearly visualized and in averaged high-definition 2-D frames where the signal to noise ratio in the deeper layers is further increased, therefore, birefringence can be detected sufficiently well for segmentation of the CSI.

The FDML laser features a relatively simple and, therefore, robust optical set-up combined with the capability of arbitrary spectral shaping. This improves the axial resolution for a given sweep bandwidth and permits using both sweep directions for OCT imaging without a buffering stage. Hence, we achieve high imaging speed while keeping the optical system complexity low.

However, uncompensated chromatic dispersion, in the long fiber resonator leads, to a rather short coherence length of the light source which, in turn, causes a fast sensitivity roll-off for OCT imaging. The FDML laser performs sufficiently well for imaging thin samples, like the retina, as we have demonstrated. However, a slower roll-off would be highly beneficial for a practical application. Slower roll-off would allow

imaging of structures spanning a longer depth range, reduce or even eliminate the residual asymmetry of the roll-off for both sweep directions, and increase the tolerance for adjusting the reference path length. Especially, the first point is crucial for introducing high-speed polarization-sensitive imaging for clinical use since, in patients, thick pathological structures might occur which can only partly be imaged with the system presented here. Additionally, it would allow the positioning of the imaged object further away of the imaging artifact that is visible in Fig. 5 which could not be removed with fixed pattern noise removal. Once these issues have been addressed by further technical development, high-speed PS-OCT, at 1060 nm, has the potential to become a valuable tool for ophthalmologic diagnostics. A possible solution might be using a concept for improving the roll-off for FDML sources which has been presented recently.[42]

Additionally, further investigation and comparison of birefringence values, in the RNFL and DOPU values, obtained from measurements with different probing wavelengths, would be interesting to see if our findings can be reproduced. Our suggestion for such a study would be to increase the number of subjects and take PS-OCT set-ups with different probing wavelengths, but with similar parameters (imaging speed, resolution, sensitivity, etc.), to ensure that observed differences are caused solely by different probing wavelengths.

References

1. D. Huang et al., "Optical coherence tomography," *Science* **254**(5035), 1178–1181 (1991).
2. A. F. Fercher et al., "Optical coherence tomography—principles and applications," *Rep. Prog. Phys.* **66**(2), 239–303 (2003).
3. W. Drexler and J. G. Fujimoto, *Optical Coherence Tomography— Technology and Applications*, Springer, Berlin (2008).
4. S. Marschall et al., "Optical coherence tomography—current technology and applications in clinical and biomedical research," *Anal. Bioanal. Chem.* **400**(9), 2699–2720 (2011).
5. W. Drexler and J. G. Fujimoto, "Optical coherence tomography in ophthalmology," *J. Biomed. Opt.* **12**(4), 041201 (2007).
6. W. Geitzenauer, C. K. Hitzenberger, and U. M. Schmidt-Erfurth, "Retinal optical coherence tomography: past, present and future perspectives," *Br. J. Ophthalmol.* **95**(2), 171–177 (2011).
7. R. Leitgeb, C. K. Hitzenberger, and A. F. Fercher, "Performance of fourier domain vs. time domain optical coherence tomography," *Opt. Express* **11**(8), 889–894 (2003).
8. J. F. de Boer et al., "Improved signal-to-noise ratio in spectral-domain compared with time-domain optical coherence tomography," *Opt. Lett.* **28**(21), 2067–2069 (2003).
9. M. A. Choma et al., "Sensitivity advantage of swept source and Fourier domain optical coherence tomography," *Opt. Express* **11**(18), 2183–2189 (2003).
10. B. Potsaid et al., "Ultrahigh speed spectral/Fourier domain OCT ophthalmic imaging at 70,000 to 312,500 axial scans per second," *Opt. Express* **16**(19), 15149–15169 (2008).
11. L. An et al., "High speed spectral domain optical coherence tomography for retinal imaging at 500,000 A-lines per second," *Biomed. Opt. Express* **2**(10), 2770–2783 (2011).
12. B. Potsaid et al., "Ultrahigh speed 1050 nm swept source/Fourier domain OCT retinal and anterior segment imaging at 100,000 to 400,000 axial scans per second," *Opt. Express* **18**(19), 20029–20048 (2010).
13. C. Blatter et al., "Ultrahigh-speed non-invasive widefield angiography," *J. Biomed. Opt.* **17**(7), 070505 (2012).
14. R. Huber, M. Wojtkowski, and J. G. Fujimoto, "Fourier domain mode locking (FDML): a new laser operating regime and applications for optical coherence tomography," *Opt. Express* **14**(8), 3225–3237 (2006).
15. N. Iftimia, B. E. Bouma, and G. J. Tearney, "Speckle reduction in optical coherence tomography by "path length encoded" angular compounding," *J. Biomed. Opt.* **8**(2), 260–263 (2003).
16. M. Pircher et al., "Speckle reduction in optical coherence tomography by frequency compounding," *J. Biomed. Opt.* **8**(3), 565–569 (2003).
17. A. Unterhuber et al., "*In vivo* retinal optical coherence tomography at 1040 nm - enhanced penetration into the choroid," *Opt. Express* **13**(9), 3252–3258 (2005).
18. Y. Yasuno et al., "*In vivo* high-contrast imaging of deep posterior eye by 1 μm swept source optical coherence tomography and scattering optical coherence angiography," *Opt. Express* **15**(10), 6121–6139 (2007).
19. E. C. W. Lee et al., "*In vivo* optical frequency domain imaging of human retina and choroid," *Opt. Express* **14**(10), 4403–4411 (2006).
20. S. Marschall, C. Pedersen, and P. E. Andersen, "Investigation of the impact of water absorption on retinal OCT imaging in the 1060 nm range," *Biomed. Opt. Express* **3**(7), 1620–1631 (2012).
21. Y. Wang et al., "Optimal wavelength for ultrahigh-resolution optical coherence tomography," *Opt. Express* **11**(12), 1411–1417 (2003).
22. S. Hariri et al., "Limiting factors to the OCT axial resolution for in-vivo imaging of human and rodent retina in the 1060 nm wavelength range," *Opt. Express* **17**(26), 24304–24316 (2009).
23. M. Esmaeelpour et al., "Three-dimensional 1060-nm OCT: choroidal thickness maps in normal subjects and improved posterior segment visualization in cataract patients," *Invest. Ophthalmol. Vis. Sci.* **51**(10), 5260–5266 (2010).
24. M. Esmaeelpour et al., "Mapping choroidal and retinal thickness variation in type 2 diabetes using three-dimensional 1060-nm optical coherence tomography," *Invest. Ophthalmol. Vis. Sci.* **52**(8), 5311–5316 (2011).
25. Y. Ikuno et al., "Reproducibility of retinal and choroidal thickness measurements in enhanced depth imaging and high-penetration optical coherence tomography," *Invest. Ophthalmol. Vis. Sci.* **52**(8), 5536–5540 (2011).
26. J. F. de Boer et al., "Two-dimensional birefringence imaging in biological tissue by polarization-sensitive optical coherence tomography," *Opt. Lett.* **22**(12), 934–936 (1997).
27. M. R. Hee et al., "Polarization-sensitive low-coherence reflectometer for birefringence characterization and ranging," *J. Opt. Soc. Am. B* **9**(6), 903–908 (1992).
28. J. F. de Boer and T. E. Milner, "Review of polarization sensitive optical coherence tomography and Stokes vector determination," *J. Biomed. Opt.* **7**(3), 359–371 (2002).
29. M. Pircher, C. K. Hitzenberger, and U. Schmidt-Erfurth, "Polarization sensitive optical coherence tomography in the human eye," *Prog. Retin. Eye Res.* **30**(6), 431–451 (2011).
30. R. N. Weinreb et al., "Histopathologic validation of Fourier-ellipsometry measurements of retinal nerve fiber layer thickness," *Arch. Ophthalmol.* **108**(4), 557–560 (1990).
31. B. Cense et al., "*In vivo* depth-resolved birefringence measurements of the human retinal nerve fiber layer by polarization-sensitive optical coherence tomography," *Opt. Lett.* **27**(18), 1610–1612 (2002).
32. H. B. klein Brink and G. J. van Blokland, "Birefringence of the human foveal area assessed *in vivo* with Mueller-matrix ellipsometry," *J. Opt. Soc. Am. A* **5**(1), 49–57 (1988).
33. M. Pircher et al., "Imaging of polarization properties of human retina *in vivo* with phase resolved transversal PS-OCT," *Opt. Express* **12**(24), 5940–5951 (2004).
34. B. Baumann et al., "Single camera based spectral domain polarization sensitive optical coherence tomography," *Opt. Express* **15**(3), 1054–1063 (2007).
35. M. Yamanari, S. Makita, and Y. Yasuno, "Polarization-sensitive swept-source optical coherence tomography with continuous source polarization modulation," *Opt. Express* **16**(8), 5892–5906 (2008).
36. M. Pircher et al., "Human macula investigated *in vivo* with polarization-sensitive optical coherence tomography," *Invest. Ophthalmol. Vis. Sci.* **47**(12), 5487–5494 (2006).
37. E. Götzinger et al., "Three-dimensional polarization sensitive OCT imaging and interactive display of the human retina," *Opt. Express* **17**(5), 4151–4165 (2009).
38. C. Ahlers et al., "Imaging of the retinal pigment epithelium in age-related macular degeneration using polarization sensitive optical coherence tomography," *Invest. Ophthalmol. Vis. Sci.* **51**(4), 2149–2157 (2010).
39. E. Götzinger et al., "Retinal pigment epithelium segmentation by polarization sensitive optical coherence tomography," *Opt. Express* **16**(21), 16410–16422 (2008).
40. L. Duan, M. Yamanari, and Y. Yasuno, "Automated phase retardation oriented segmentation of chorio-scleral interface by polarization sensitive optical coherence tomography," *Opt. Express* **20**(3), 3353–3366 (2012).
41. T. Torzicky et al., "Automated measurement of choroidal thickness in the human eye by polarization sensitive optical coherence tomography," *Opt. Express* **20**(7), 7564–7574 (2012).
42. D. Adler et al., "Extended coherence length Fourier domain mode locked lasers at 1310 nm," *Opt. Express* **19**(21), 20930–20939 (2011).
43. T. Klein et al., "Megahertz OCT for ultrawide-field retinal imaging with a 1050 nm Fourier domain mode-locked laser," *Opt. Express* **19**(4), 3044–3062 (2011).
44. B. R. Biedermann et al., "Real time en face Fourier-domain optical coherence tomography with direct hardware frequency demodulation," *Opt. Lett.* **33**(21), 2556–2558 (2008).
45. B. R. Biedermann et al., "Dispersion, coherence and noise of Fourier domain mode locked lasers," *Opt. Express* **17**(12), 9947–9961 (2009).
46. T. Torzicky et al., "High-speed retinal imaging with polarization-sensitive OCT at 1040 nm," *Optom. Vis. Sci.* **89**(5), 585–92 (2012).
47. E. Götzinger et al., "Speckle noise reduction in high speed polarization sensitive spectral domain optical coherence tomography," *Opt. Express* **19**(15), 14568–14585 (2011).
48. E. Götzinger, M. Pircher, and C. K. Hitzenberger, "High speed spectral domain polarization sensitive optical coherence tomography of the human retina," *Opt. Express* **13**(25), 10217–10229 (2005).
49. C. K. Hitzenberger et al., "Measurement and imaging of birefringence and optic axis orientation by phase resolved polarization sensitive optical coherence tomography," *Opt. Express* **9**(13), 780–790 (2001).

50. E. Götzinger et al., "Retinal nerve fiber layer birefringence evaluated with polarization sensitive spectral domain OCT and scanning laser polarimetry: a comparison," *J. Biophoton.* **1**(2), 129–139 (2008).

51. M. Yamanari et al., "Phase retardation measurement of retinal nerve fiber layer by polarization-sensitive spectral-domain optical coherence tomography and scanning laser polarimetry," *J. Biomed. Opt.* **13**(1), 014013 (2008).

52. A. W. Dreher, K. Reiter, and R. N. Weinreb, "Spatially resolved birefringence of the retinal nerve-fiber layer assessed with a retinal laser ellipsometer," *Appl. Opt.* **31**(19), 3730–3735 (1992).

53. M. Pircher et al., "Corneal birefringence compensation for polarization sensitive optical coherence tomography of the human retina," *J. Biomed. Opt.* **12**(4), 041210 (2007).

54. B. Cense et al., "Thickness and birefringence of healthy retinal nerve fiber layer tissue measured with polarization-sensitive optical coherence tomography," *Invest. Ophthalmol. Vis. Sci.* **45**(8), 2606–2612 (2004).

55. M. Mujat et al., "Autocalibration of spectral-domain optical coherence tomography spectrometers for *in vivo* quantitative retinal nerve fiber layer birefringence determination," *J. Biomed. Opt.* **12**(4), 041205 (2007).

56. N. J. Kemp et al., "High-sensitivity determination of birefringence in turbid media with enhanced polarization-sensitive optical coherence tomography," *J. Opt. Soc. Am.* **22**(3), 552–560 (2005).

57. B. Elmaanaoui et al., "Birefringence measurement of the retinal nerve fiber layer by swept source polarization sensitive optical coherence tomography," *Opt. Express* **19**(11), 10252–10268 (2011).

58. S. Zotter et al., "Large-field high-speed polarization sensitive spectral domain OCT and its applications in ophthalmology," *Biomed. Opt. Express* **3**(11), 2720–2732 (2012).